Materials and Design 146 (2018) 116–124

Contents lists available at ScienceDirect

Materials and Design

journal homepage: www.elsevier.com/locate/matdes

In situ synthesized TiC/Mo-based composites via laser powder bed fusion

Weiwei Zhou [a], Xiaohao Sun [a], Keiko Kikuchi [a], Naoyuki Nomura [a,*], Kyosuke Yoshimi [b], Akira Kawasaki [a,*]

[a] Department of Materials Processing, Graduate School of Engineering, Tohoku University, Sendai, Miyagi 980-8579, Japan
[b] Department of Materials Science, Graduate School of Engineering, Tohoku University, Sendai, Miyagi 980-8579, Japan

HIGHLIGHTS

- A novel strategy utilizing carbon nanotubes was put forward to synthesize in situ TiC/Mo-based composites via laser powder bed fusion.
- Carbon nanotubes were well mixed with MoTiAl powders under electrostatic attraction during heteroagglomeration process.
- In situ TiC, possessing two unique structures, namely spherical and dendritic TiC, was uniformly dispersed in the matrix.
- The MoTiAl matrix underwent a morphological change from nearly columnar to fine equiaxed grains after incorporating TiC.

GRAPHICAL ABSTRACT

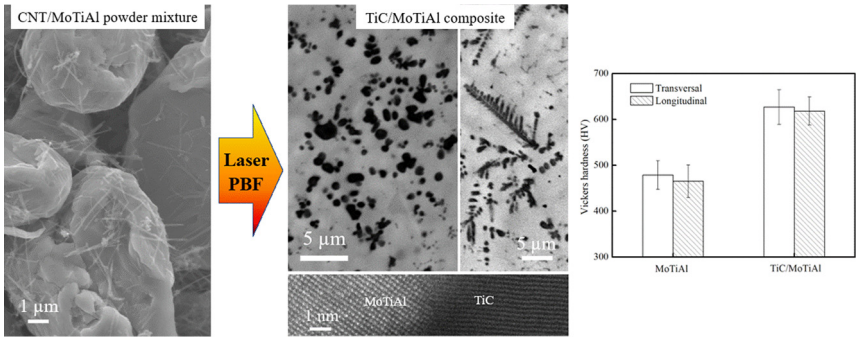

ARTICLE INFO

Article history:
Received 4 December 2017
Received in revised form 28 February 2018
Accepted 1 March 2018
Available online 6 March 2018

Keywords:
Laser powder bed fusion (laser PBF)
Metal matrix composites (MMCs)
Carbon nanotubes
Molybdenum
Microstructure

ABSTRACT

A strategy utilizing carbon nanotubes (CNTs) was put forward to synthesize in situ TiC/Mo-based composites via laser powder bed fusion (laser PBF). The functionalized CNTs were dispersed with MoTiAl powders under electrostatic attraction by heteroagglomeration. During laser PBF, individual CNTs reacted with Ti elements and were completely transformed into monocrystalline TiC. Those TiC reinforcements were homogeneously dispersed and intimately contacted the matrix, giving rise to the morphological evolution of a MoTiAl matrix from the nearly columnar to fine equiaxed grains as well as improved mechanical performance. Our finding offers significant guidance for designing and producing advanced Mo-based composites in the application of heat-resistant materials.

1. Introduction

The increasing demand for new ultra-high-temperature materials beyond the realm of Ni-based superalloys has generated significant interest in refractory intermetallics [1,2]. Owing to the high melting point and superior stiffness, Mo alloys possess promising potential in the fields of aeronautics and astronautics [3]. Unfortunately, the application reliability of Mo alloys is seriously hindered by their insufficient elevated-temperature strength [2]. In this regard, stiff and fine ceramic particles were utilized to strengthen Mo alloys by impeding the dislocation movement [4,5]. Among various ceramic reinforcements, TiC is particularly attractive for its excellent properties, such as low density (~4.93 g/cm^3), high melting point (~3430 K), high Young's modulus (~440 GPa), and good thermal stability [6,7]. Yoshimi et al. [5,8] reported that incorporating TiC into a ternary MoSiB alloy resulted in higher mechanical strength and creep resistance at elevated

* Corresponding authors.
E-mail addresses: nnomura@material.tohoku.ac.jp (N. Nomura), kawasaki@material.tohoku.ac.jp (A. Kawasaki).

https://doi.org/10.1016/j.matdes.2018.03.001
0264-1275/

Table 1
Characteristics of acid-treated CNTs and MoTiAl and 1.2 wt% CNT/MoTiAl powders.

Powders	Composition	Particle size	Zeta potential	Laser absorptivity (λ = 1070 nm)
CNTs	Fe < 0.3 wt%, C: Bal.	Diameter: 20–110 nm, length: 2–15 μm	−51.3 mV	89.8%
MoTiAl	Ti ~ 33 wt.%, Al ~ 13 wt%, Mo: Bal.	D_{10} ~ 5.1 μm, D_{50} ~ 12.8 μm, D_{90} ~ 24.9 μm	Positive, weak	71.6%
1.2 wt% CNT/MoTiAl	–	D_{10} ~ 5.3 μm, D_{50} ~ 13.0 μm, D_{90} ~ 24.2 μm	–	77.9%

temperatures via traditional casting. However, such traditional manufacturing techniques usually have some drawbacks, e.g., the insufficient densification rate and the aggregation and irregular microstructure of reinforcements, as well as the occurrence of interfacial cracking, being harmful for the mechanical performance of composites [8–10]. Furthermore, the traditional approaches involve highly time-, energy-, and material-consuming processing steps to achieve the final products [11]. Particularly, Mo alloys with poor ambient-temperature ductility are challenging to machine for complex structures.

Laser powder bed fusing (Laser PBF) is newly capable of fabricating three-dimensional products with almost uninhibited freedom of design [12]. The product is directly built using a high-energy laser beam to fuse and consolidate the loose powders selectively according to the corresponding computer-aided design models in a layer-by-layer manner [12,13]. Due to its flexibility in materials and processing, laser PBF offers new technological opportunities for producing high-performance metal matrix composites (MMCs) with tailored structures. In recent years, the laser-PBF processing of MMCs, including Al- [14–19], Ti- [20–24], Ni- [10,25–27], and Fe-based alloys [28–30], has been documented. In most cases, the reinforcements were directly added to the metallic powders by mechanical milling/blending, followed by laser PBF to create an ex situ composite. However, the poor wettability and interfacial strength between the reinforcements and metal usually cause microcracks and even premature failure of the composites [9]. In contrast, the in situ reinforcements synthesized by chemical reactions are extremely effective for composite strengthening, since they are fine and thermodynamically stable, having clean and compatible interfaces with the matrix [7,9]. AlMangour et al. [7] prepared in situ TiC/316L stainless steel composites with enhanced mechanical properties through the laser-PBF processing of 316L-Ti-graphite powder mixtures. Li et al. [22] found that the in situ TiB_2 reinforcement dramatically enhanced the nanohardness of TiB_2/TiAl composites via laser PBF. Unfortunately, to the best of our knowledge, the fabrication of in situ Mo-based composites by laser PBF has never been reported.

CNTs are considered to be ideal reinforcements for MMCs due to their low density, large aspect ratios, and excellent mechanical properties [31,32]. Recently, Chen et al. [33] synthesized high-strength Al_4C_3/Al composites via the in situ reaction of CNTs with Al during spark plasma sintering. Herein, an idea is put forward to develop high-performance Mo-based composites by transforming CNTs into TiC reinforcements during laser PBF, based on the following considerations: (i) after a surface modification, individual CNTs could wrap on the surface of metallic powders easily under electrostatic attraction without severe fabrication processing [34]; (ii) CNTs still possess excellent load-bearing capability in MMCs, even though the reaction is incomplete, e.g., Wang et al. [27] reported that incorporation of CNTs enhanced the mechanical properties of PBF-produced Inconel 625 parts; and (iii) compared with using large graphite sheets [7,35], using CNTs may allow the formation of fine TiC structures for enhanced strengthening. In this work, a TiC reinforcement was synthesized in situ via laser PBF; its microstructural characteristics and effect on the morphology and mechanical properties of Mo alloy were investigated.

2. Experimental

2.1. Raw materials

A simple Mo-33wt%Ti-13wt%Al solid solution was chosen as one example of Mo alloys in this work [36]. The starting MoTiAl powders having an irregular shape (Fig. S1 of Supporting information), were fabricated via a combination of arc melting, mechanical milling and sieving, and their size distribution of D_{10}, D_{50} and D_{90} were 5.1 μm, 12.8 μm and 24.9 μm, respectively (Table 1). Pristine CNTs having a diameter of 20–110 nm and a length of 2–15 μm were provided by Hodogaya Chemical Co., Ltd., Japan. The high-purity ethanol, sulfuric acid (H_2SO_4, 97 wt%) and nitric acid (HNO_3, 61 wt%) were obtained from Wako Industries, Japan.

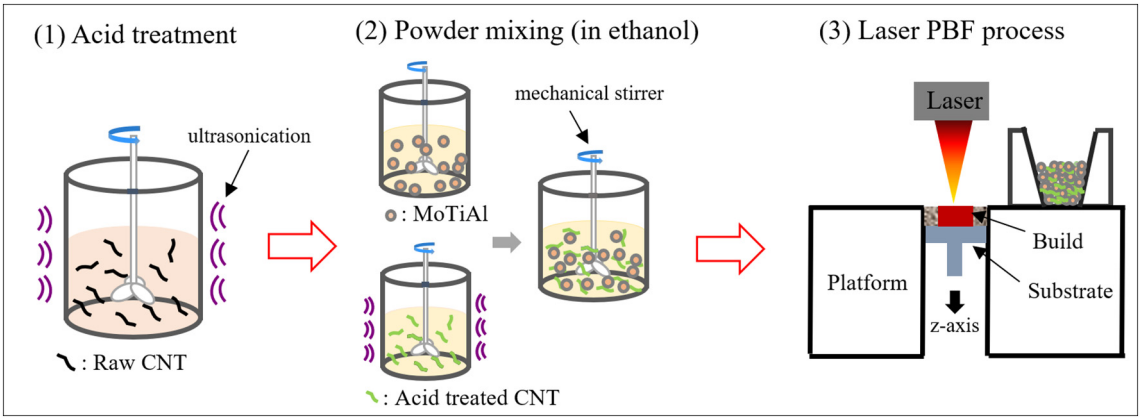

Fig. 1. Schematic illustration of the fabrication processes for Mo-based composites.

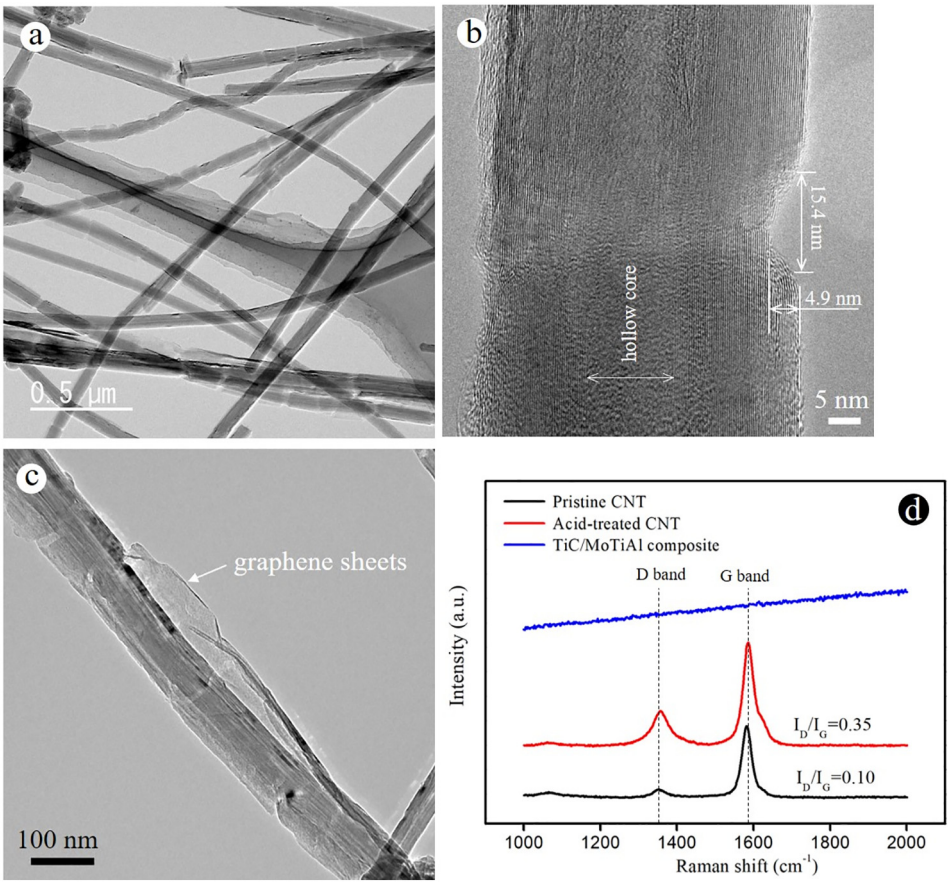

Fig. 2. (a–c) TEM images of the acid-treated CNT; (d) Raman spectra of pristine CNT, acid-treated CNT, and the PBF-produced TiC/MoTiAl composite.

2.2. Fabrication of CNT/MoTiAl composite powders

A schematic illustration of our processing strategy is shown in Fig. 1. Firstly, the surface of pristine CNTs was sufficiently functionalized by a mild acid treatment to break the strong agglomerates of CNTs. As reported elsewhere [37], the pristine CNTs were initially purified by HNO_3 for 12 h, and then treated in an acidic mixture of H_2SO_4/HNO_3 (3:1, v/v) under mechanical stirring and ultrasonication at 323 K for 6 h. After that, 0.036 g CNTs and 2.964 g MoTiAl powders were separately dispersed into 100 ml and 300 ml of ethanol for 2 h. Subsequently, the MoTiAl slurry was added slowly into a CNT colloid under mechanical blending. After filtration and drying at 343 K in a vacuum environment, the 1.2 wt% CNT/MoTiAl composite powders were obtained.

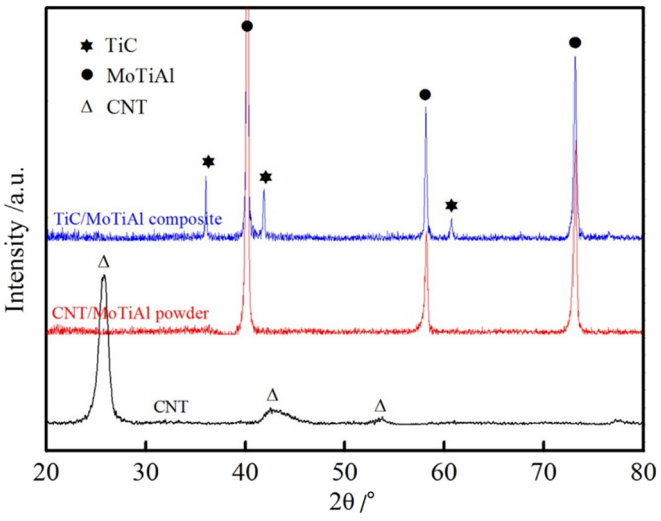

Fig. 3. XRD patterns of acid-treated CNTs, CNT/MoTiAl powders, and the PBF-produced TiC/MoTiAl composite.

2.3. Laser PBF process

An in-house-developed laser-PBF machine (see Fig. 1), equipped with a Yb: YAG fiber laser source (Raycus Fiber Laser Technologies Co., Ltd., China), was used to produce bulk specimens. The laser beam has a wavelength of 1070 nm, spot diameter of 45 μm, and maximum power of 22 W in continuous mode. The building process was performed under protective Ar atmosphere with a low oxygen content (<0.1%). The fabricated specimens had a rectangular shape of 4 mm × 4 mm × 1.4 mm on a Ti substrate. Both pure MoTiAl and CNT/MoTiAl composite powders were processed by using the optimized parameters of laser PBF (i.e., laser power: 20.6 W; scanning speed: 25 mm s^{-1}; hatch distance: 100 μm; layer thickness: 25 μm; X–Y alternately scanning strategy).

2.4. Characterization

The zeta potential of powders was measured in ethanol using a zeta meter (Malvern Instruments Ltd., UK). The laser absorptivity measurements were performed on a V-670 UV–VIS-NIR spectrophotometer (JASCO, Japan). The X-ray diffraction (XRD) was conducted using a

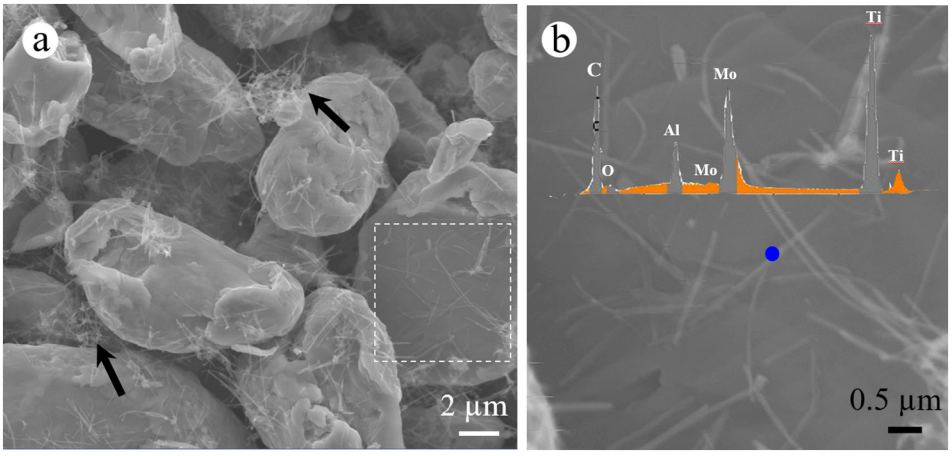

Fig. 4. FESEM images of the 1.2 wt% CNT/MoTiAl composite powders. (b) is taken from the position of white square in (a). The inset in (b) shows the energy dispersive spectroscope analysis taken from the blue spot.

Rigaku Smartlab 9 kW diffractometer with Cu Kα radiation. The surface of PBF builds was mechanically grinded by sandpapers from 180# to 4000#, followed by a final polishing using the standard colloidal silica suspension (OP-S, Struers); subsequently, the polished surface was analyzed by micro-Raman spectrum (SOLAR TII Nanofinder, Tokyo Instruments Co. Ltd.) with 532 nm wavelength incident laser light and 5 μm spot size for at least ten times. The morphologies of powders or PBF bulks were observed via field-emission scanning electron microscope (FESEM) (JEOL JSM-6500F), electron back-scattered diffraction (EBSD) (OIM ver. 6, TSL Solutions, Japan), electron probe micro-analysis (EPMA) (JEOL JXA-8530F, Japan), transmission electron microscopy (TEM) (Hitachi HF-2000EDX, Japan), and annular-dark-field scanning transmission electron microscopy (STEM) (JEOL JEM-ARM200F, Japan) equipped with an energy dispersive spectroscope at 200 KeV. TEM bulk specimens were prepared using a focused ion beam (JEOL JIB-4600F) system. Vickers hardness measurements were performed using a digital hardness tester (HM-200, Mitutoyo, Japan) at room temperature, according to ISO standard 14577-1:2015. The indenter was continuously loaded to the peak load of 0.6 N in 10 s and unloaded after a holding time of 10 s.

3. Results and discussion

Structural features of the acid-treated CNTs are displayed in Fig. 2. The CNTs are relatively straight, showing a high aspect ratio (Fig. 2a). Fig. 2b reveals that certain nanodefects ~5 nm deep and ~15 nm wide were induced on the sidewalls of CNTs by acid treatment. Furthermore, the outer walls of CNTs were partially unzipped for producing graphene sheets (Fig. 2c). Micro-Raman spectroscopy is a powerful tool to characterize sp^2 carbonaceous materials and evaluate defects in their structures. Two prominent features in the first-order Raman spectroscopy are a G-band at about 1580 cm^{-1} as the graphite mode, and a D-band at about 1350 cm^{-1} as the defect mode. Due to the introduced structural disorders, the I_D/I_G ratio of pristine CNTs increased from 0.10 to 0.35 after acid treatment (Fig. 2d). However, the acid-treated CNT still remained a typical hollow structure, as well as the continuous and parallel inner walls along the axial direction showed high crystallinity (see Fig. 2b). This result is further confirmed by the XRD analysis in Fig. 3, since the characteristic diffraction peaks of CNTs were observed clearly. It is known that the perfect CNT is chemically stable; no reaction occurs, even in contact with molten metal [38]. The produced nanodefects and graphene sheets involve many dangling bonds of carbon atoms; they are deemed to be the preferential reaction sites with the MoTiAl matrix.

Thanks to abundant oxygen-containing surface groups [37], the CNTs were hydrophilic and exhibited a significantly negative charge of −51.3 mV (Table 1), making them attach to the positively charged MoTiAl powders by electrostatic attraction during powder mixing. Morphologies of the 1.2 wt% CNT/MoTiAl powders are displayed in Fig. 4. Individual CNTs were well dispersed on the surface of MoTiAl powders. Few CNT clusters (see black arrows in Fig. 4a) were detected at this concentration of 1.2 wt%; this is mainly attributed to the large particle size but weak surface charge of MoTiAl powders.

In addition to good dispersion of nano-reinforcements, the composite powders fabricated by our heteroagglomeration process could remain similar in shape, particle size, and distribution to starting metallic particles for laser PBF, compared with commonly used high-energy ball milling. Furthermore, the laser absorptivity of MoTiAl powders increased from 71.6% to 77.9% with CNT addition of 1.2 wt% (Table 1), which may improve the laser-PBF processability of Mo alloys.

Typical microstructures of a PBF-produced composite are displayed in Figs. 5–8. Neither unmelted MoTiAl particles nor visible pores were present in this composite. However, some microcracks were detected (see black arrow in Fig. 8a), which were mainly attributed to the brittle nature of Mo alloys, as well as severe thermal and residual stresses arising from the high thermal gradient or inhomogeneous plastic deformation at rapid cooling (10^{-3}–10^{-8} Ks^{-1}) [15,39]. As revealed by FESEM-backscattered electron observations in Fig. 5a and b, many secondary particulates (i.e., the dark phases) were incorporated and dispersed uniformly throughout the composite. The EPMA mappings proved that those particulates mainly consist of elemental Ti and C (Fig. 5c), corresponding to TiC. This result is consistent with XRD analysis; the strong and sharp diffraction peaks of TiC crystals were identified after laser PBF (Fig. 3).

Further microstructural analysis was performed by annular-dark-field STEM. Fig. 6b and c illustrate the selected-area electron diffraction patterns of TiC (yellow spot) along the [111] zone axe and MoTiAl matrix (blue spot) along the [−110] zone axe of Fig. 6a. As revealed by high-resolution STEM (Fig. 6d), this TiC is highly crystalline and free of dislocation lines and atomic disorders, suggesting a sufficient release of internal stress during its formation. Obviously, the in situ TiC has two typical morphologies distinctly different from the initial CNT, as shown in Fig. 5a and b. The dominant one is a fine, nearly spherical particle (see yellow arrows) 0.1–2 μm in diameter. The average distance between two adjacent TiC particles was ~1 μm (Fig. 6d). The other is a dendritic TiC (see green arrows), which has a dendrite trunk length of 5–20 μm and an arm length of 0.1–5 μm. Fig. 7 shows typical example of a dendric TiC by STEM. The corresponding selected-area electron

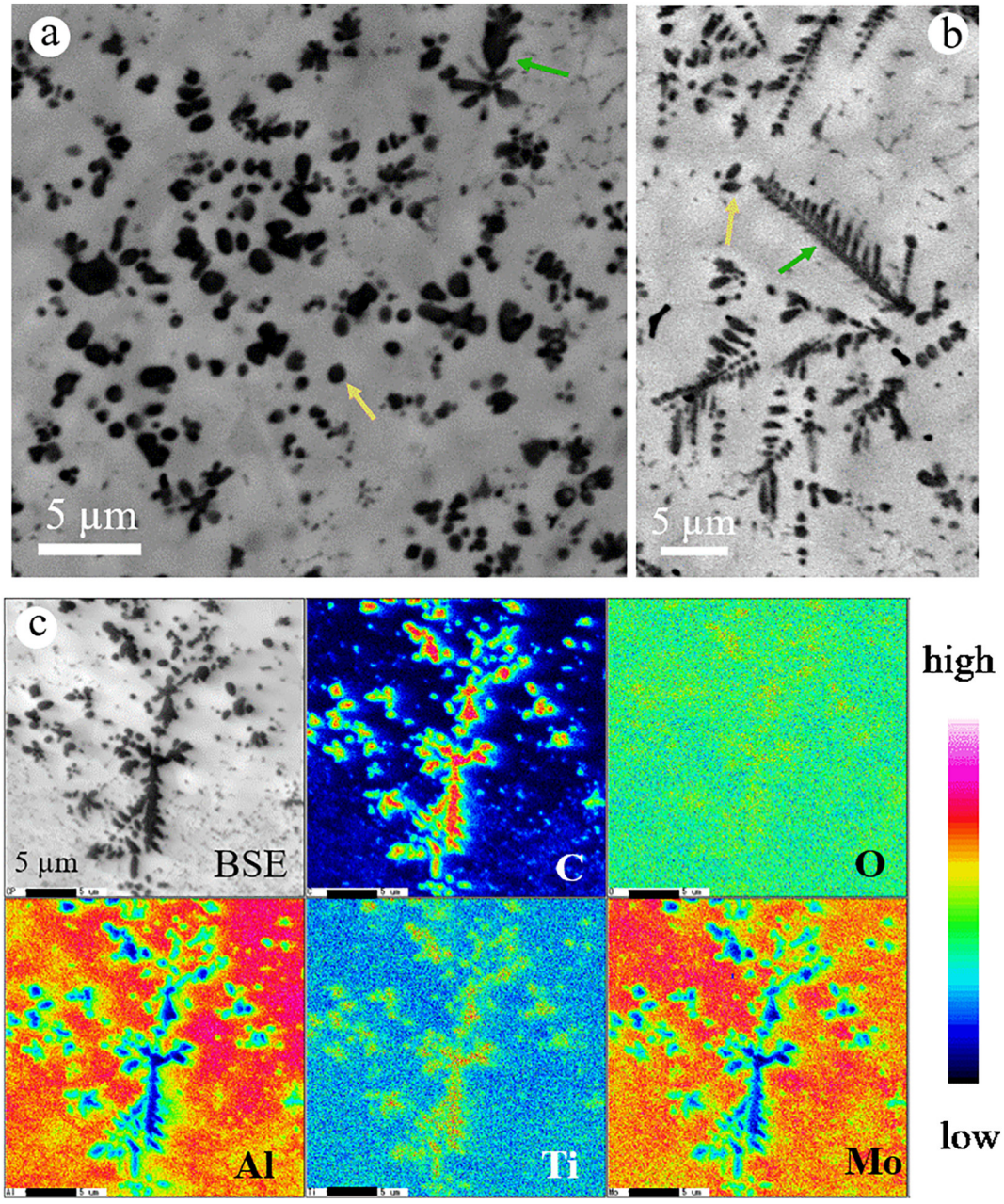

Fig. 5. (a, b) FESEM-backscattered electron images and (c) EPMA mappings of the PBF-produced TiC/MoTiAl composite in the transversal cross section.

diffraction patterns demonstrated that both nearly spherical and dendric TiC structures are monocrystalline with a face-centered cubic structure (see Figs. 6 and 7). In addition, no residual CNTs were detected in this composite via careful STEM observations. The characteristic features of CNTs were not identified by micro-Raman spectroscopy as well (see Fig. 2d). It suggests that CNTs were completely transformed to TiC during laser PBF.

In an Al-Ti-C system, TiC was generated at temperatures of over 1191 K [40]. During laser PBF, CNTs with higher laser absorptivity would be heated to a higher temperature than their surrounding molten MoTiAl (>2073 K [36]), facilitating the possibility of a chemical reaction: C + Ti → TiC. This reaction is an exothermic, self-sustaining, and rapid process driven by the large negative enthalpy of TiC formation (−184.5 kJ/mol) [40,41]. Since the in situ TiC did not retain the tube shape of the CNT, it is thought that nano-TiC was preferentially formed between dangling carbon atoms and Ti elements, followed by growth through an inter-diffusion process [6].

When the CNT/MoTiAl composite powders involve small amount of CNTs (e.g., <0.5 wt%), the dendrite TiC was barely observed after laser PBF [34]; in contrast, a large quantity of dendrite TiC was formed with increasing the CNT content (Fig. S2, Supporting information). Accordingly, the nearly spherical TiC should stem from individual CNTs, while the CNT clusters contain rich C atoms beneficial to the successive growth of dendrite TiC. Due to the thermal stresses induced plastic flow during laser PBF, the TiC crystals were rearranged and distributed homogenously in the matrix [35,42].

Fig. 6d illustrates a clear TiC/MoTiAl interface. Notably, this interface is extremely tight and clean, absent of interfacial impurities or nanocracks. This is mainly attributed to the similar coefficients of thermal expansion between TiC (~5.9 × 10^{-6} K^{-1} [43]) and Mo

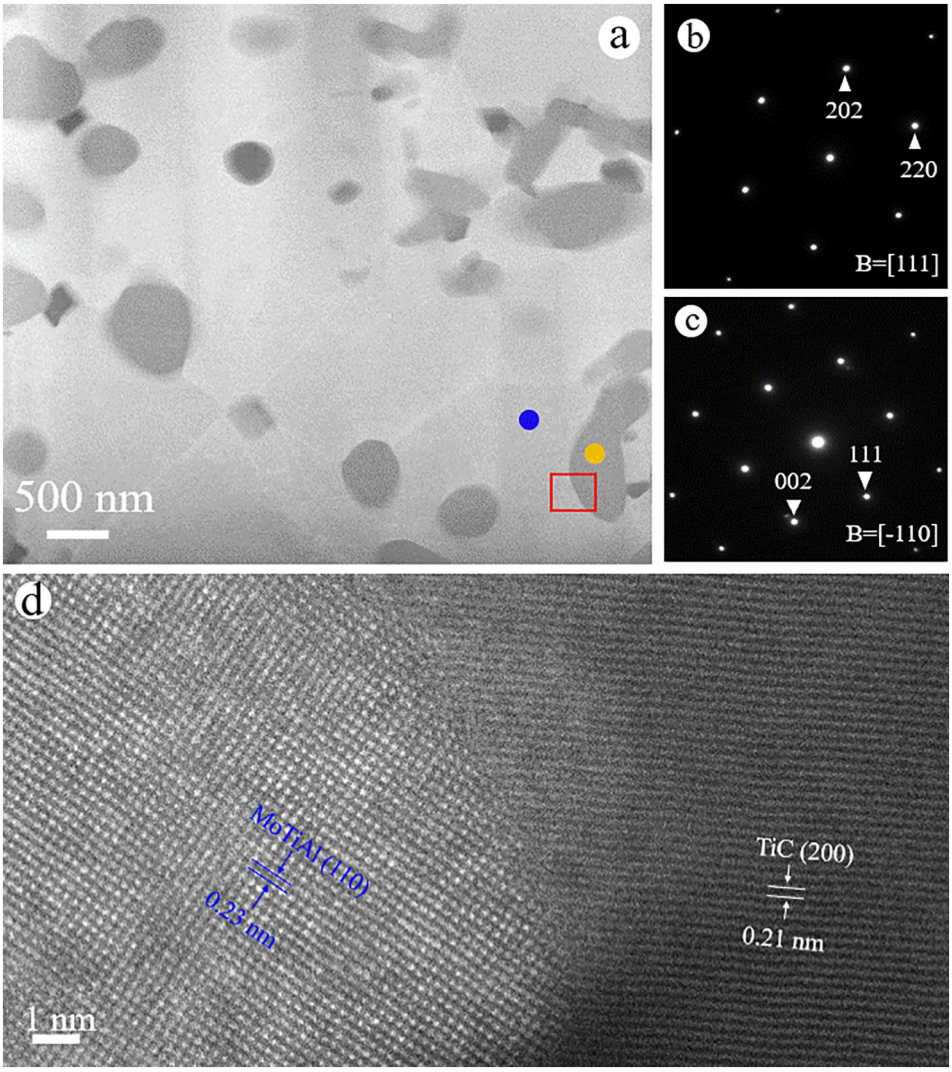

Fig. 6. (a) Annular-dark-field STEM image of TiC/MoTiAl composite in the transversal cross section; selected-area electron diffraction patterns of (b) TiC and(c) MoTiAl taken from the yellow and blue spots in (a), respectively; (d) high-resolution STEM image taken from the position of the red square in (a).

(~4.8×10^{-6} K^{-1} [44]), as well as their interfacial wettability enhanced by in situ reaction.

The influence of in situ TiC on the crystallization behavior of the MoTiAl matrix was investigated via EBSD analysis. Fig. 8a shows pure MoTiAl having nearly columnar grains. That is mainly owing to the high thermal gradient arise from rastering of a direct laser energy source in an arbitrary geometric pattern, as well as an insufficient undercooling during the solidification of molten pools [45]. Strikingly, those columnar MoTiAl grains were transformed into a uniform equiaxed structure after incorporating TiC (Fig. 8b). Meanwhile, the mean grain size decreased from 14.2 μm to 3.3 μm (Fig. 8d). The EBSD phase mappings determined that the quantity of TiC formation in this composite was approximately 11.1 vol% (Fig. 8c), which is similar to the expected value assuming that CNTs were completely reacted to TiC structures during laser PBF. Such a high density of TiC was expected to reduce the critical amount of undercooling required for equiaxed grains by providing low-energy-barrier heterogeneous nucleation sites ahead of the solidification front, as well as to hinder MoTiAl grain growth by the pinning effects of TiC dispersions. Our result is well consistent with the study of Martin et al. [46] that introducing nanoparticles of nucleants contributed to producing crack-free MMCs with equiaxed, fine-grained microstructures. Compared with the coarse columnar grains, the fine equiaxed structures could more effectively accommodate strains and prevent crack initiation and propagation under loading. Our processing strategy may provide an effective approach to control solidification microstructure of Mo alloys, thus giving rise to an enhanced mechanical performance.

Fig. 9 displays the Vickers hardnesses of PBF-processed MoTiAl and the TiC/MoTiAl composite. The Vickers hardnesses of pure MoTiAl were measured to be 478.6 ± 31.2 and 465.2 ± 35.4 in the transversal and longitudinal cross sections, respectively. The Vickers hardnesses of the TiC/MoTiAl were 626.9 ± 37.8 and 618.3 ± 30.5 in the transversal and longitudinal cross sections, respectively. Hall [47] proposed that the hardness, H, dependence on grain size, d, might follow from the Hall-Petch relation, thus the hardness-grain size relation is described by

$$H = H_0 + K_H d^{-1/2}, \quad (1)$$

where H_0, K_H are constants associated with the hardness measurement. In this work, K_H was determined as 227.8 $\mu m^{-1/2}$ (see Table S1 and Fig. S3). According to Eq. (1), the Vickers hardness of TiC/MoTiAl composite in the transversal cross section was assumed to be 543.6, which is much lower the experimental value. This indicates that the dispersion strengthening of in situ synthesized TiC should be mainly attributed to

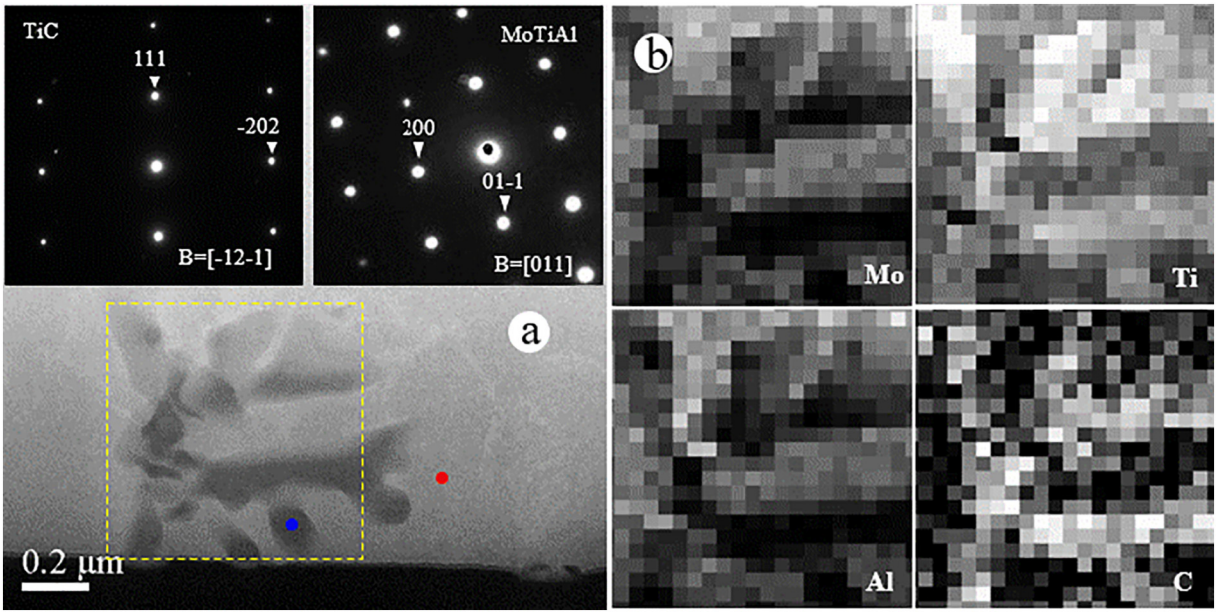

Fig. 7. (a) Annular-dark-field STEM image of a typical dendric TiC; (b) the corresponding energy dispersive spectroscope mappings of elemental Mo, Ti, Al, C taken from the position of yellow square in (a). The insets in (a) show the selected-area electron diffraction patterns of TiC and MoTiAl matrix taken from the blue and red spots, respectively.

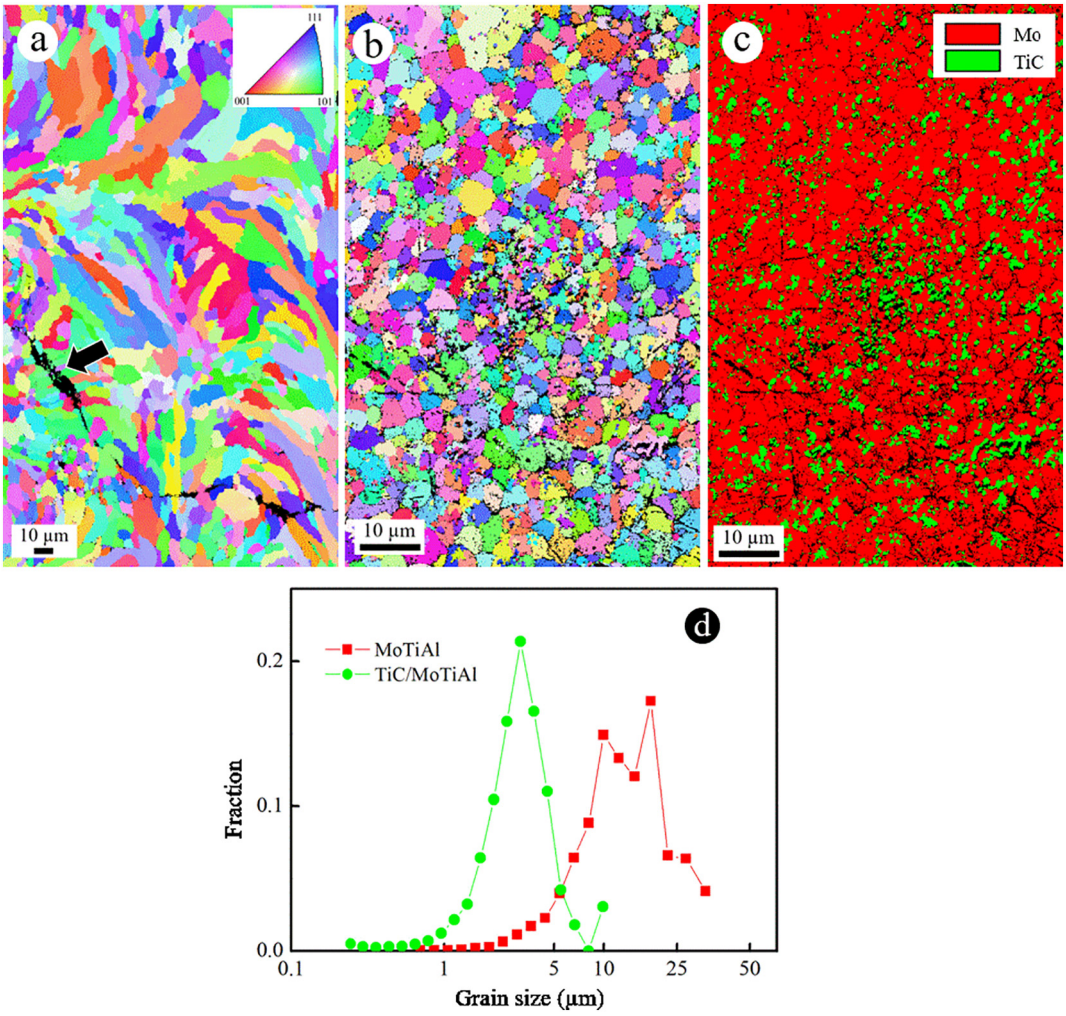

Fig. 8. Inverse pole figures of (a) PBF-produced MoTiAl and (b) a TiC/MoTiAl composite in the transversal cross sections; (c) phase mapping of the TiC/MoTiAl composite from (b); (d) grain-size distribution of MoTiAl and the TiC/MoTiAl composite in the transversal cross sections.

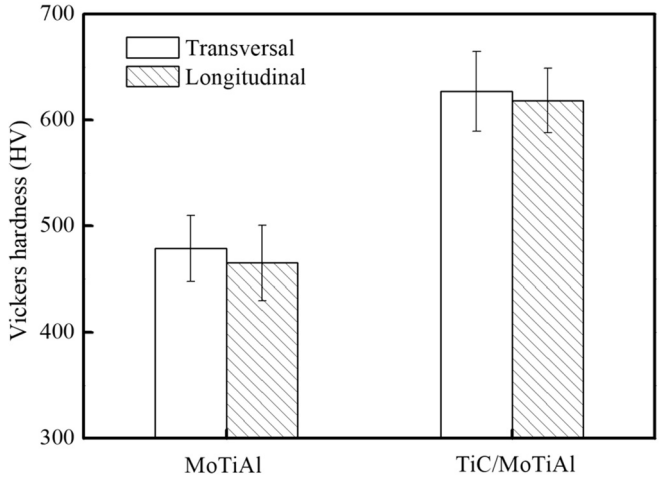

Fig. 9. Vickers hardnesses of PBF-produced pure MoTiAl and TiC/MoTiAl composite in the transversal and longitudinal cross sections.

the hardness improvement of the composite. The influence of TiC formation (e.g., morphology and quantity) on the microstructural evolution and elevated-temperature properties of Mo alloys will be systematically investigated in future work.

4. Conclusions

In summary, we have fabricated an in situ TiC/MoTiAl composite by utilizing CNTs during laser PBF. The functionalized CNTs were mixed with MoTiAl powders under electrostatic attraction by heteroagglomeration. During laser PBF, CNTs reacted with Ti atoms and were completely transformed into TiC. The in situ TiC exhibited two unique structures, namely fine, nearly spherical and dendritic TiC, different from the initial CNTs. Meanwhile, the TiC reinforcements were monocrystalline and uniformly dispersed, showing an intimate contact with the matrix. Furthermore, the MoTiAl matrix underwent an interesting morphological change from nearly columnar to fine equiaxed grains, simultaneously showing a dramatic improvement in Vickers hardness after incorporating TiC. This finding will be a valuable reference for fabricating advanced Mo-based composites with controlled microstructures and enhanced mechanical properties via laser PBF.

Acknowledgment

This work was supported by the New Energy and Industrial Technology Department Organization (NEDO) in Japan through the Energy and Environment New Technology Leading Program. The authors thank Dr. Takamichi Miyazaki and Dr. Kosei Kobayashi for the technical assistance in the TEM analysis.

Appendix A. Supplementary data

Supplementary data to this article can be found online at https://doi.org/10.1016/j.matdes.2018.03.001.

References

[1] T.A. Parthasarathy, M.G. Mendiratta, D.M. Dimiduk, Oxidation mechanisms in Mo-reinforced Mo5SiB2(T2)–Mo3Si alloys, Acta Mater. 50 (2002) 1857–1868.
[2] D.M. Dimiduk, J.H. Perepezko, Mo-Si-B alloys: developing a revolutionary turbine-engine material, MRS Bull. 28 (2003) 639–645.
[3] M. Krüger, S. Franz, H. Saage, M. Heilmaier, J. Schneibel, P. Jéhanno, M. Böning, H. Kestler, Mechanically alloyed Mo–Si–B alloys with a continuous α-Mo matrix and improved mechanical properties, Intermetallics 16 (2008) 933–941.
[4] G. Liu, G. Zhang, F. Jiang, X. Ding, Y. Sun, J. Sun, E. Ma, Nanostructured high-strength molybdenum alloys with unprecedented tensile ductility, Nat. Mater. 12 (2013) 344–350.
[5] S. Miyamoto, K. Yoshimi, S.-H. Ha, T. Kaneko, J. Nakamura, T. Sato, K. Maruyama, R. Tu, T. Goto, Phase equilibria, microstructure, and high-temperature strength of TiC-added Mo-Si-B alloys, Metall. Mater. Trans. A 45 (2014) 1112–1123.
[6] D. Gu, Y.C. Hagedorn, W. Meiners, K. Wissenbach, R. Poprawe, Nanocrystalline TiC reinforced Ti matrix bulk-form nanocomposites by selective laser melting (SLM): densification, growth mechanism and wear behavior, Compos. Sci. Technol. 71 (2011) 1612–1620.
[7] B. AlMangour, D. Grzesiak, J.-M. Yang, In-situ formation of novel TiC-particle-reinforced 316L stainless steel bulk-form composites by selective laser melting, J. Alloys Compd. 706 (2017) 409–418.
[8] M. Zhao, S. Nakayama, T. Hatakeyama, J. Nakamura, K. Yoshimi, Microstructure, high-temperature deformability and oxidation resistance of a Ti5Si3-containing multiphase MoSiBTiC alloy, Intermetallics 90 (2017) 169–179.
[9] S.C. Tjong, Novel nanoparticle-reinforced metal matrix composites with enhanced mechanical properties, Adv. Eng. Mater. 9 (2007) 639–652.
[10] T. Rong, D. Gu, Formation of novel graded interface and its function on mechanical properties of WC 1−x reinforced Inconel 718 composites processed by selective laser melting, J. Alloys Compd. 680 (2016) 333–342.
[11] D.D. Gu, W. Meiners, K. Wissenbach, R. Poprawe, Laser additive manufacturing of metallic components: materials, processes and mechanisms, Int. Mater. Rev. 57 (2012) 133–164.
[12] S. Bremen, W. Meiners, A. Diatlov, Selective laser melting, Laser Tech. J. 9 (2012) 33–38.
[13] L. Thijs, F. Verhaeghe, T. Craeghs, J. Van Humbeeck, J.-P. Kruth, A study of the microstructural evolution during selective laser melting of Ti–6Al–4V, Acta Mater. 58 (2010) 3303–3312.
[14] D. Gu, H. Wang, D. Dai, P. Yuan, W. Meiners, R. Poprawe, Rapid fabrication of Al-based bulk-form nanocomposites with novel reinforcement and enhanced performance by selective laser melting, Scr. Mater. 96 (2015) 25–28.
[15] X.P. Li, C. Kong, T. Becker, T. Sercombe, Investigation of interfacial reaction products and stress distribution in selective laser melted Al12Si/SiC composite using confocal Raman microscopy, Adv. Eng. Mater. 18 (2016) 1337–1341.
[16] Q.Q. Han, R. Setchi, S.L. Evans, Synthesis and characterisation of advanced ball-milled al-Al2O3 nanocomposites for selective laser melting, Powder Technol. 297 (2016) 183–192.
[17] J.B. Jue, D.D. Gu, Selective laser melting additive manufacturing of in situ Al2Si4O10/Al composites: microstructural characteristics and mechanical properties, J. Compos. Mater. 51 (2017) 519–532.
[18] L.M. Laorden, P. Rodrigo, B. Torres, J. Rams, Modification of microstructure and superficial properties of A356 and A356/10%SiCp by selective laser surface melting (SLSM), Surf. Coat. Technol. 309 (2017) 1001–1009.
[19] L. Wang, F. Qiu, Q. Zhao, H. Wang, Q. Jiang, Simultaneously increasing the elevated-temperature tensile strength and plasticity of in situ nano-sized TiCx/Al-Cu-Mg composites, Mater. Charact. 125 (2017) 7–12.
[20] H. Attar, M. Bönisch, M. Calin, L.C. Zhang, S. Scudino, J. Eckert, Selective laser melting of in situ titanium–titanium boride composites: processing, microstructure and mechanical properties, Acta Mater. 76 (2014) 13–22.
[21] D. Gu, G. Meng, C. Li, W. Meiners, R. Poprawe, Selective laser melting of TiC/Ti bulk nanocomposites: influence of nanoscale reinforcement, Scr. Mater. 67 (2012) 185–188.
[22] W. Li, Y. Yang, J. Liu, Y. Zhou, M. Li, S.F. Wen, Enhanced nanohardness and new insights into texture evolution and phase transformation of TiAl/TiB2 in-situ metal matrix composites prepared via selective laser melting, Acta Mater. 136 (2017) 90–104.
[23] B.B. He, K. Chang, W.H. Wu, C.L. Zhang, The formation mechanism of TiC reinforcement and improved tensile strength in additive manufactured Ti matrix nanocomposite, Vacuum 143 (2017) 23–27.
[24] L.C. Zhang, H. Attar, Selective laser melting of titanium alloys and titanium matrix composites for biomedical applications: a review, Adv. Eng. Mater. 18 (2016) 463–475.
[25] Q. Jia, D. Gu, Selective laser melting additive manufacturing of TiC/Inconel 718 bulk-form nanocomposites: densification, microstructure, and performance, J. Mater. Res. 29 (2014) 1960–1969.
[26] Y. Wang, J. Shi, S. Lu, Y. Wang, Selective laser melting of graphene-reinforced Inconel 718 superalloy: evaluation of microstructure and tensile performance, J. Manuf. Sci. Eng. 139 (2016) 041005-1–041005-6.
[27] P. Wang, B. Zhang, C.C. Tan, S. Raghavan, Y.F. Lim, C.N. Sun, J. Wei, D.Z. Chi, Microstructural characteristics and mechanical properties of carbon nanotube reinforced Inconel 625 parts fabricated by selective laser melting, Mater. Des. 112 (2016) 290–299.
[28] B. Song, S. Dong, C. Coddet, Rapid in situ fabrication of Fe/SiC bulk nanocomposites by selective laser melting directly from a mixed powder of microsized Fe and SiC, Scr. Mater. 75 (2014) 90–93.
[29] B. AlMangour, D. Grzesiak, Selective laser melting of TiC reinforced 316L stainless steel matrix nanocomposites: influence of starting TiC particle size and volume content, Mater. Des. 104 (2016) 141–151.
[30] B. Song, Z.W. Wang, Q. Yan, Y.J. Zhang, J.L. Zhang, C. Cai, Q.S. Wei, Y.S. Shi, Integral method of preparation and fabrication of metal matrix composite: selective laser melting of in-situ nano/submicro-sized carbides reinforced iron matrix composites, Mater. Sci. Eng., A 707 (2017) 478–487.
[31] W. Zhou, G. Yamamoto, Y. Fan, H. Kwon, T. Hashida, A. Kawasaki, In-situ characterization of interfacial shear strength in multi-walled carbon nanotube reinforced aluminum matrix composites, Carbon 106 (2016) 37–47.

[32] W. Zhou, T. Yamaguchi, K. Kikuchi, N. Nomura, A. Kawasaki, Effectively enhanced load transfer by interfacial reactions in multi-walled carbon nanotube reinforced Al matrix composites, Acta Mater. 125 (2017) 369–376.
[33] B. Chen, L. Jia, S. Li, H. Imai, M. Takahashi, K. Kondoh, In situ synthesized Al4C3 nanorods with excellent strengthening effect in aluminum matrix composites, Adv. Eng. Mater. 16 (2014) 972–975.
[34] W. Zhou, X. Sun, K. Kikuchi, N. Nomura, K. Yoshimi, A. Kawasaki, Carbon nanotubes as a unique agent to fabricate nanoceramic/metal composite powders for additive manufacturing, Mater. Des. 137 (2017) 276–285.
[35] D. Gu, Z. Wang, Y. Shen, Q. Li, Y. Li, In-situ TiC particle reinforced Ti–Al matrix composites: powder preparation by mechanical alloying and selective laser melting behavior, Appl. Surf. Sci. 255 (2009) 9230–9240.
[36] Y. Lu, J. Yamada, J. Nakamura, K. Yoshimi, H. Kato, Effect of B2-ordered phase on the deformation behavior of Ti-Mo-Al alloys at elevated temperature, J. Alloys Compd. 696 (2017) 130–135.
[37] W.W. Zhou, S. Sasaki, A. Kawasaki, Effective control of nanodefects in multiwalled carbon nanotubes by acid treatment, Carbon 78 (2014) 121–129.
[38] L. Ci, Z. Ryu, N.Y. Jin-Phillipp, M. Rühle, Investigation of the interfacial reaction between multi-walled carbon nanotubes and aluminum, Acta Mater. 54 (2006) 5367–5375.
[39] P. Krakhmalev, I. Yadroitsev, Microstructure and properties of intermetallic composite coatings fabricated by selective laser melting of Ti–SiC powder mixtures, Intermetallics 46 (2014) 147–155.
[40] T. Nukami, M.C. Flemings, In situ synthesis of TiC particulate-reinforced aluminum matrix composites, Metall. Mater. Trans. A 26 (1995) 1877–1884.
[41] F. Akhtar, Microstructure evolution and wear properties of in situ synthesized TiB 2 and TiC reinforced steel matrix composites, J. Alloys Compd. 459 (2008) 491–497.
[42] S. Dadbakhsh, L. Hao, Effect of Al alloys on selective laser melting behaviour and microstructure of in situ formed particle reinforced composites, J. Alloys Compd. 541 (2012) 328–334.
[43] G.M. Song, Y.-J. Wang, Y. Zhou, Thermomechanical properties of TiC particle-reinforced tungsten composites for high temperature applications, Int. J. Refract. Met. Hard Mater. 21 (2003) 1–12.
[44] F. Nix, D. MacNair, The thermal expansion of pure metals. II: molybdenum, palladium, silver, tantalum, tungsten, platinum, and lead, Phys. Rev. 61 (1942) 74.
[45] B. Song, S. Dong, P. Coddet, H. Liao, C. Coddet, Fabrication of NiCr alloy parts by selective laser melting: columnar microstructure and anisotropic mechanical behavior, Mater. Des. (2014) 1–7.
[46] J.H. Martin, B.D. Yahata, J.M. Hundley, J.A. Mayer, T.A. Schaedler, T.M. Pollock, 3D printing of high-strength aluminum alloys, Nature 549 (2017) 365–369.
[47] E.O. Hall, Variation of hardness of metals with grain size, Nature 173 (1954) 948–949.